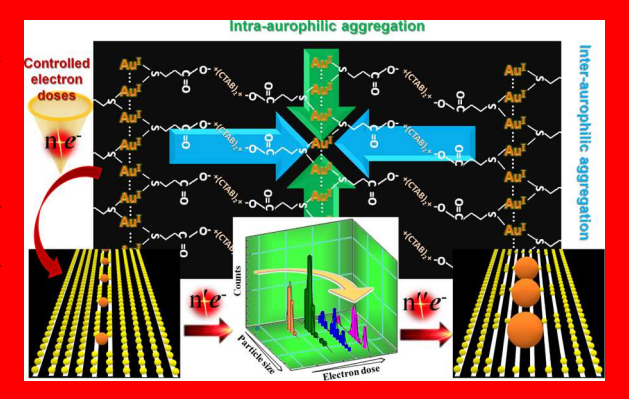


# Electron Dose-Controlled Formation, Growth, and Assembly of Nanoclusters and Nanoparticles from Aurophilic Au(I)—Thiolate **Ensemble on Surfaces**

Han-Wen Cheng,\*,†,‡ Shan Yan,‡ Jing Li,‡ Jie Wang,§ Lingyan Wang,¶ Zakiya Skeete,‡ Shiyao Shan,‡ and Chuan-Jian Zhong\*,‡0

Supporting Information

The ability to precisely control electron irradiationinduced formation, growth, and assembly of nanoclusters or nanoparticles on a solid surface is important for design and creation of catalytically or chemically active surface sites and interfaces free from chemical reducing agents. Here, we show the results of an investigation of the electron dose-controlled formation, growth, and assembly of nanoclusters and nanoparticles in a molecularly assembled thin film of Au(I)-thiolate motifs on a substrate, highlighting an in situ monitoring of the evolution of morphology under controlled electron dose. With aurophilic motifs of Au(I)thiolate being confined by electrostatic interactions, the sizes of Au nanoclusters and nanoparticles were shown to increase with electron dose, revealing a propensity of a string alignment of the grown nanoclusters and nanoparticles. This growth preference to one-



dimensional assembly is supported by the analysis of the surface reaction kinetics in terms of the surface density of electron dose for the growth of the nanoclusters and nanoparticles. The electron dose-controlled size-focusing and directional assembly of nanoclusters and nanoparticles may be exploited as new strategy for the precise control of nanoclusters or nanoparticles and their assemblies on solid surfaces not only free from chemical reducing agent but also with the ability of visual monitoring of the morphological evolution during growth.

electron dose, aggregative growth, in situ monitoring, one-dimensional assembly, aurophilic Au(I)—SR motifs. and gold nanoclusters and nanoparticles

# INTRODUCTION

Although electron irradiation has been utilized as a chemical agent-free source for the reduction of oxidized metals in solutions to form nanoparticles (NPs), the understanding has largely involved solution-based redox reactions. Few studies have involved investigating the NPs formed by electron irradiation-induced reduction processes in thin films or nanostructured materials on solid surfaces. The increasing interests in the synthesis of nanostructured materials and thin films of metal nanoclusters (NCs) or NPs toward atomic level control in catalysis, electrocatalysis, chemical sensing, biosensing, and theranotics have captured a wide range of interests in the development of abilities to control the size and assembly of NCs or NPs on solid surfaces. These interests focus on exploring their individual or ensemble functional properties. NCs or NPs derived by gold (Au)-thiolate (SR) chemistry in solutions<sup>2-11</sup> have been studied, especially involving the

conventional two-phase synthesis by wet chemical reduction which converts Au(III) to Au(I),  $[Au(I)-S(R)]_n$ , and Au NCs or NPs. The so-called Au(I)-SR staple motifs, which are formed by reducing Au(III) to Au(I), 12-18 have found potential applications in catalysis and medical theranostics 19,20 and in constructing therapeutic agents through exploiting the aurophilic interactions. 21,22 The rich chemistry of Au-SR motifs has also been highlighted by the ability of thiolmediated etching of gold NPs in solutions for creating "atomically precise" clusters. 23-25 Despite the progress made in understanding of the redox chemistry of Au(I)-thiolate motifs to produce thiolate-protected gold NCs or NPs in some solutions, little attention has been paid to the nanoscale

Received: October 14, 2018 Accepted: October 24, 2018 Published: November 6, 2018



<sup>&</sup>lt;sup>†</sup>School of Chemical and Environmental Engineering, Shanghai Institute of Technology, Shanghai 201418, China

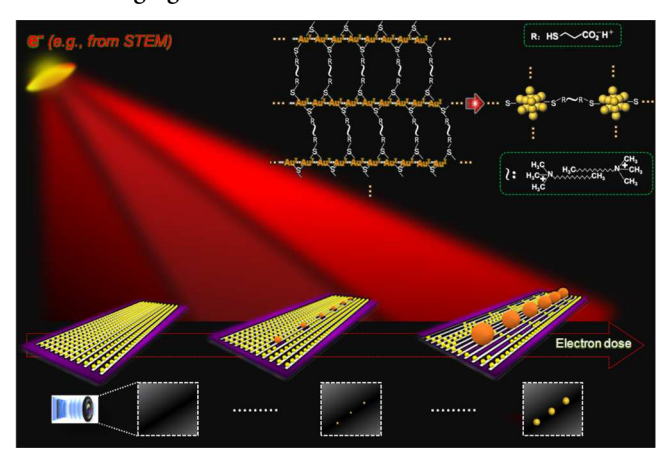
<sup>&</sup>lt;sup>‡</sup>Department of Chemistry, State University of New York at Binghamton, Binghamton, New York 13902, United States

<sup>§</sup>Electron & X-ray Microscopy, Nanoscience and Technology, Argonne National Laboratory, Lemont, Illinois 60439, United States Corning Incorporated, New York 14831, United States

chemistry of Au-SR motifs in thin films or nanostructures under direct exposure to electrons.

We have recently demonstrated the intriguing viability of NC and NP formation and assembly from Au(I)-thiolate motifs using electron beams from the source of electron microscopy, which are typical tools used for visualizing the detailed structures of NCs or NPs. 26 The significance of this initial finding was the ability to exploit the nanoscale assembly of NCs or NPs from thin films of Au-thiolate motifs under direct exposure to electrons as the sole agent, which could constitute an ideal pathway for triggering and driving the nanoscale reactions and assemblies.<sup>27-34</sup> Being motivated by the unprecedented directional preference in the assembly, we demonstrate here for the first time an in situ monitoring of formation and one-dimensional assembly of NCs or NPs from Au(I)-SR motifs in molecularly assembled thin films as a function of electron dose by the electron beam from scanning transmission electron microscopy (STEM). As illustrated in Scheme 1, the control of electron doses serves an intriguing

Scheme 1. Schematic Illustration of the Use of Controlled Electron Doses in Formation, Growth, and Assembly of NCs and NPs from Aurophilic Motifs of Au(I)-Thiolate on Solid Substrate and the Visual Monitoring through, e.g., STEM Imaginga



<sup>a</sup>The upper-right inset illustrates the motifs in an electrostatically bound structure consisting of, e.g., a cationic cetyltrimethylammonium and anionic mercaptopropionic carboxylate. The lower panel illustrates in situ monitoring of the morphological evolution at different electron doses.

pathway for the formation, growth, and assembly of NCs or NPs on a substrate surface. As an example, molecularly assembled aurophilic Au-thiolate motifs<sup>26</sup> are placed on a solid surface via an electrostatically bound structure consisting of, for example, positively charged cetyltrimethylammonium bromide (CTAB) and negatively charged mercaptopropionic acid (MPA).

There are different methods to synthesize Au(I)-thiolate complexes.  $^{7,35}$  Etching of presynthesized gold NPs capped with cationic CTAB using anionic MPA is one of the methods to produce Au(I)—thiolate species. <sup>23–25</sup> This method enables the exploitation of the cationic-anionic electrostatic interaction as a template in the assembly of the resulting Au(I)-thiolate species. The long-chain cationic CTAB provides an electrostatic structure for part of the template. With this type of nanostructures on a solid surface, a fundamental question is

how the inter- and intra-autophilic interactions of the Au(I)thiolate motifs in the presence of positively charged CTAB and negatively charged MPA interactions define the network chemical reactivity. This understanding is essential for exploring Au(I)-thiolate aurophilic network as a pathway toward creating one-dimensional assemblies of NCs or NPs with tunable catalytic, sensing, and diagnostic functions. In this report, the results of an in situ STEM study focusing on monitoring the nanoscale chemistry of the Au(I)-SR motifs in the molecularly assembled thin film under different electron doses have provided a new insight into the electron-induced size-focusing and directional assembly of NCs and NPs. The understanding of the mechanistic details of the electron dose dependence is expected to provide the precise control of NCs or NPs and their assemblies not only free from chemical reducing agent but also with the ability of visual monitoring of the morphological evolution during the growth. Considering previous studies of electron doses for the reduction of oxidized metal ions in solutions to form NPs, the knowledge obtained from the present work would also be useful for preparing thiolate-protected gold NCs in solutions by electron irradiation with controlled electron dose, especially in view of recent reports on atomically precise NCs, step-by-step reaction processes,<sup>35</sup> and stoichiometric synthesis of water-soluble NCs in terms of the number of electrons from reducing agents.<sup>3</sup>

# **EXPERIMENTAL SECTION**

Chemicals. Tetrachloroauric(III) acid (HAuCl<sub>4</sub>·3H<sub>2</sub>O), 3-mercaptopropionic acid (MPA, 99+%), and sodium borohydride (NaBH<sub>4</sub>) were obtained from Sigma-Aldrich. CTAB (>98%) was obtained from Alfa Aesar. Ethanol (>99.5%) and methanol (>99.9%) were purchased from Fisher Scientific. All reagents were used as received. Deionized water from Mill-Q water (18 M $\Omega$ ·cm) was used.

Synthesis and Preparation. Au NPs were first synthesized by a typical aqueous one-phase synthesis method,<sup>37</sup> which involved the reduction of HAuCl<sub>4</sub> in the presence of CTAB by NaBH<sub>4</sub>. CTABcapped Au NPs were produced. Depending on the reaction time (10 min to 40 h), Au NPs of 2-6 nm in diameter were obtained. This process involved forming Au(I)-SR via etching the as-synthesized NPs.<sup>23,24,38</sup> Typically, a solution of MPA was added to the solution of the CTAB-capped Au NPs and the etching reaction was allowed to proceed 15 h to form Au(I)-thiolate in the solution. The resulting Au(I)-thiolate species were then subject to centrifugation twice and redispersion in water.

Characterization and Measurement. We used high-angle annular dark-field (HAADF) STEM, TEM, and energy-dispersive Xray spectroscopy (EDS) for the characterizations.

JEOL JEM 2010F instrument was used to obtain TEM images under 200 kV. The fluorescent screen of TEM measures 10-20 pA/ cm<sup>2</sup> for regular and high-resolution (HR) imaging at 200 kV. Exposure time for regular TEM is ~0.5 s.

FEI Titan G2 80-200 instrument with ChemiSTEM capability was used to obtain STEM and EDS element mapping under 200 kV. A combination of condenser lenses and apertures was used to control the current density and the convergence angle of the electron beam. The collection of HAADF images was performed in STEM mode under a small camera length which ensures that the annular dark-field detector detects only the electrons deflected by angles greater than 50 mrad. For STEM, the screen current for energy-dispersive X-ray mode is around 0.5 nA on most magnifications. The probe current on each pixel in a STEM image is 0.5 nA. The image setting is 2048 pixels  $\times$ 2048 pixels, and the dwell time is 8  $\mu$ s. For a specific imaging area, the dose rate in unit of A/nm<sup>2</sup> or e/nm<sup>2</sup> s could be calculated. For a higher magnification, that is, a smaller imaging area, there is a higher dose rate, either in terms of the average dose rate over the entire imaging frame, or the peak dosage on each pixel. The calculation of electron dose/scan is performed by multiplying electron dose rate by

the number of the image's pixels and the pixel dwell time. Note that the time for the focused e beam to rest on a single pixel is defined as the pixel dwell time. Therefore, the longer the pixel time, the more the electrons can be collected per pixel, and the lower the scan speed will be (e.g., an image that is 2048 and 2048 pixels in width and height has a total of  $2048 \times 2048 = 4.2$  megapixels). Note that the equipment is typically calibrated to the detector efficiency ranging from 10 to 90%, and the detector dose rate is an estimate depending on the specific instrument. Considering that the actual exposure also depends on the time being spent in collecting the data, a series of TEM images and STEM image were acquired from a specific area within a controlled time, which allowed us to assess the morphological evolution as a function of the total electron dose.

UV-vis spectrophotometry measurements were also carried out to determine the plasmonic and electronic properties of the assynthesized NPs or NCs in the solutions, which were obtained on a Hewlett Packard 8453 UV-vis spectrophotometer. Electrospray ionization (ESI) nanospray time-of-flight (TOF) mass spectra were collected with a Qstar XL mass spectrometer (MDS Sciex, Applied Biosystems) with an ion spray voltage of 800 V, where the sample was dispersed into methanol with addition of trace NaOH to increase the opportunity of ionization. Physical Electronics 5000 versa probe scanning ESCA was used for X-ray photoelectron spectroscopy (XPS) characterization. In this system, a focused monochromatic Al Klpha Xray (1486.7 eV) source was used for excitation. The binding energy scale was calibrated using the Cu  $2p_{3/2}$  line at 932.58  $\pm$  0.05 eV and the Au  $4f_{7/2}$  line at 84.01  $\pm$  0.05 eV.

# **RESULTS AND DISCUSSION**

Au(I)-SR motifs were prepared by etching presynthesized Au NPs of about 2 or 6 nm diameter (Scheme S1), 23,24,26 which were first synthesized by reducing AuCl<sub>4</sub><sup>-</sup> in the presence of CTAB  $(CH_3(CH_2)_{15}N(CH_3)^+_3Br^-)$  with  $NaBH_4$  in the aqueous solution. MPA (HS(CH<sub>2</sub>)<sub>2</sub>CO<sub>2</sub>H, or H-SR) was used as an etchant and a re-capping agent. The formation of Au(I)-SR as the etching product was confirmed by optical absorption, in which the plasmonic resonance bands (~500, and ~540 nm) characteristic of 2 and 6 nm Au NPs disappeared. In the meantime, the bands at 288, 342-345, and 383-387 nm characteristic of Au(I)-SR were detected (Figure S1). It was also supported by ESI-nanospray TOF mass spectroscopic detection of Au(I)-species.<sup>26</sup> The Au-S (from MPA) chemistry of the Au(I)-S species was also confirmed by XPS analysis, in which the Au  $4f_{7/2}$  and  $4f_{5/2}$  were detected at 84.7 and 88.6 eV, and the S 2p<sub>3/2</sub> and 2p<sub>1/2</sub> were observed at 163.6 and 164.7 eV, respectively (Figure S2). Note that there were still some NPs remaining in the etching solution because the NPs were not completely etched.<sup>26</sup> The remaining NPs were used as an internal reference for in situ STEM analysis of sampling areas without NPs, as shown in this report.

Morphological Characteristics of NCs and NPs Formed by Electron Dose. We have recently shown that the Au(I)-SR motifs could be grown into NCs or NPs under electron beams from TEM and STEM.<sup>26</sup> The quantitative growth of NCs and NPs in string or random distributions under controlled electron doses was analyzed by taking a series of STEM image from a specific imaging area within controlled current and time. The morphological evolution was then assessed in terms of its relationship with electron dose. The division of the beam's current by the size of imaging area yields the electron dose rate  $(R_{\rm ed})^{39}$ 

$$R_{\rm ed} = i_{\rm e}/eA \tag{1}$$

where  $R_{\rm ed}$  stands for electron dose rate with the unit of electrons/ $Å^2$  s,  $i_e$  stands for beam current with the unit of C/s, and A stands for scan area in  $Å^2$ . The multiplication of  $R_{\rm ed}$  by the dwell time and the pixel number gives the electron dose/ scan. The electron dose (D), or surface density of the electron dose, is defined as the product of the current density  $(i_e)$  and the irradiation time (t).

$$D = i_{c}t \tag{2}$$

For HAADF imaging in STEM mode, the image intensity is proportional to the mass<sup>41</sup> in terms of contrast in a single scan. It is known that the average dose under STEM ( $D_{av} = 150 \text{ C}$ m<sup>-2</sup>) could be controlled at a much smaller dose than that delivered in TEM mode ( $D_{\rm av} = 1.2 \times 10^7~{\rm C~m}^{-2}$ ), yielding a ratio [ $D_{\rm av}$  (TEM)/ $D_{\rm av}$  (STEM)] of  $\sim 10^4.40$  The charge conservation through an electron beam exposure region of a typical sample 42 involves the total electron current entering the exposed volume, including the current of the main electron beam and the current created by the electrons from the regions surrounding the exposed volume that might flow into it. This is equal to the charges leaving the volume, 43 including the current from the transmitted beam, the electrons produced by the beam-specimen interaction, the electrons from the interaction volume, and the rate of charge accumulated in the exposed volume.

It was the morphological evolution of Au(I)-SR samples under high electron dose TEM that has captured our initial interest in electron lacing of NCs and NPs.<sup>26</sup> The overall string and bundling morphologies of the observed NCs or NPs were found to be highly dependent on the electron source. In the case of electron source from TEM, the strings of NCs and NPs observed under low magnifications in relatively large imaging areas, that is, lower electron dose, showed a feature resembling a bamboo leave with extensive bundling (Figure S3a,b).<sup>26</sup> An analysis of the average string diameter  $(d_0)$ , string-to-string gap  $(d_1)$ , and NC-to-NC (or NP-to-NP) gap in a string  $(d_2)$ showed 5.7 nm  $(d_0)$ , 5.2 nm  $(d_1)$ , and 3.7 nm  $(d_2)$  (Figure S4a). As the magnification increases, or imaging area decreases or electron dose increases, the sizes of the NCs or NPs increase along the strings, which is shown in Figure 1a. A similar feature was also observable in Figure S3c. The analysis of the size parameters showed 7.9 nm  $(d_0)$ , 3.9 nm  $(d_1)$ , and  $d_2$  4.7 nm  $(d_2)$  (Figure S4b).

The resulting NPs showed a clear preference of alignment in strings or bundled strings, which is schematically illustrated in Figures 1b and S3d. To understand the origin of the NC or NP formation, growth, and alignment, samples were examined

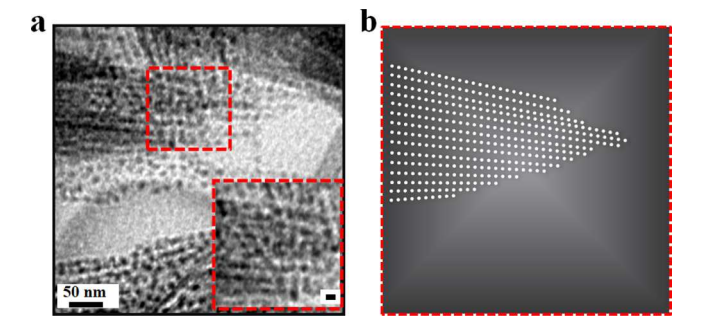


Figure 1. (a) TEM image acquired under a high magnification. Inset is a magnified view showing the indicated region (scale bar: 10 nm). (b) Schematic illustration of the bundling of NP strings in image a.

under STEM condition, where the electron dose could be controlled more precisely than TEM in terms of the imaging size (or magnification) and fixed exposure time, which are discussed next.

For a given sample that is exposed to an electron beam, the electron dose is represented by the number of electrons within specific area and time. By increasing the speed of scan (i.e., reducing the pixel dwell time), the electron dose could be reduced during image acquisition. This is a major difference of STEM from TEM. A representative set of HR-HAADF STEM images for Au(I)-SR on TEM grid is shown in Figure 2. The

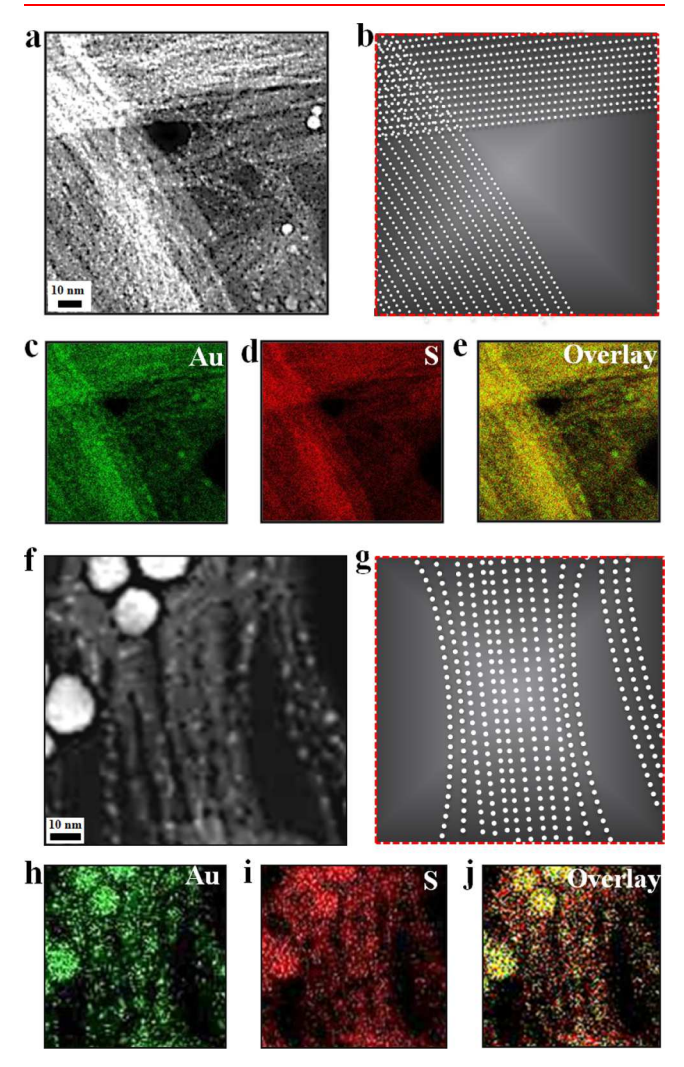


Figure 2. STEM images of a sample obtained by MPA etching of presynthesized Au NPs capped with CTAB with two different sizes [2 (a) and 6 nm (f)]. (b,g) Schematic illustrations of the bundling of NC strings in image (a) (b), and image (f) (g). (c-e,h-j) Mapping of the bundled NC strings by EDS: (c,h) Au, (d,i) S, and (e,j) S and Au overlapping.

images (Figure 2a,f) revealed bundles of strings of NCs (1-2 nm or less), as schematically illustrated in Figure 2b,g. Largersized NPs are scattered in the image, which is due to incomplete etching. These NPs served as an image contrast reference. NCs and strings are evident in Figure 2a, displaying 1.2 nm  $(d_0)$ , 1.5 nm  $(d_1)$ , and 1.4 nm  $(d_2)$  (see Figure S5a). There is a high degree of overlapping of the strings, that is, bundling. In the presence of larger-sized NPs, the NCs in

Figure 2f display similar values, 1.3 nm  $(d_0)$ , 1.4 nm  $(d_1)$ , and 1.7 nm  $(d_2)$  (see Figure S5b), with a similar bundling of the strings.

EDS mapping analysis was performed to determine the chemical composition of the bundled NC strings, displaying mainly S and Au in Figure 2c-e,h-j. These bundled Au NC strings were derived from Au(I)-MPA precursors. These strings are remarkably aligned in the presence of MPA and CTAB, as supported by larger-area STEM/EDS analyses (Figure S6) which revealed large patches of species with C and O. The Au(I)-MPA in the CTAB and MPA matrix likely consist of Au(I)-S(CH<sub>2</sub>)<sub>2</sub>CO<sub>2</sub><sup>-</sup> (with Na<sup>+</sup>) and Au(I)-S(CH<sub>2</sub>)<sub>2</sub>CO<sub>2</sub><sup>-</sup> (with CTAB<sup>+</sup>). The fact that both S and Au were clearly detected for the etched product (Figure S7d), in contrast to the detection of only Au for the sample before etching (see Figure S7a-c), further confirm the identity of the Au(I)-SR species.

The above results clearly demonstrated the propensity from Au(I)-thiolate species to form NCs/NPs in a strong distribution under the electron dose. The NCs in the strings are separated and individually identifiable. It is the MPA-CTAB network structure that provides a template environment for the alignment of Au(I)-SR motifs and the resulting NCs/

In Situ Monitoring of Morphological Changes by **Different Electron Doses.** The morphological evolution of the NCs/NPs in the strings or those in random distributions are closely monitored in terms of electron doses by varying the imaging area with fixed current (0.5 nA) and time (8  $\mu$ s/pixel). Figure 3a-e,j-n shows a representative set of STEM images, including bright and dark field images, to show the formation and growth of NCs/NPs in strings. The electron dose was controlled by the imaging area, ranging from  $1 \times 10^6$  to  $6 \times$ 10<sup>3</sup> nm<sup>2</sup>. The detailed growth profiles for the individual NCs/ NPs were extracted from the images with different imaging areas by zooming the selected areas with the two larger-sized NPs as an internal reference. While there are no indications of NCs for the imaging area above  $\sim 2 \times 10^6$  nm<sup>2</sup> (Figure 3a,b,jk), NCs/NPs are observed for imaging areas smaller than that, and the particle size show an apparent increase with the decrease in imaging area or the increase in electron dose (Figure 3c-e,l-n). Apparently, some of the particles grow by its own, whereas others grow by aggregation of smaller particles nearby. This assessment is evidenced by the zoomed views of the NCs in Figure 3c-e (Figure 3g-i). There is a preference for the alignment of the resulting NCs/NPs along

By very close examination, some of the small NCs form and grow into larger ones while other NCs undergo aggregative growth into larger ones as the electron dose increases. As indicated by the final NPs labeled I-IV (Figure 3i) and tracking of the growth of the NCs/NPs preceding them (Figure 3g-h), it is evident that aggregative growth of NCs/ NPs in close vicinity appears to be dominant along the string, in addition to display of a gradual growth from small to larger size for some of the NCs/NPs. The strings of NCs in Figure 3e exhibit 1.9 nm  $(d_2)$  (see Figure S8), which is very similar to that determined based on the data for the bundled strings of NCs [1.7 nm  $(d_2)$ ] (see Figure 2f).

To further understand the above observations of NC/NP growth along the string and develop an assessment on the detailed growth mechanism of NCs/NPs, the evolution of NCs/NPs in areas with random distributions under different

**ACS Applied Materials & Interfaces** 

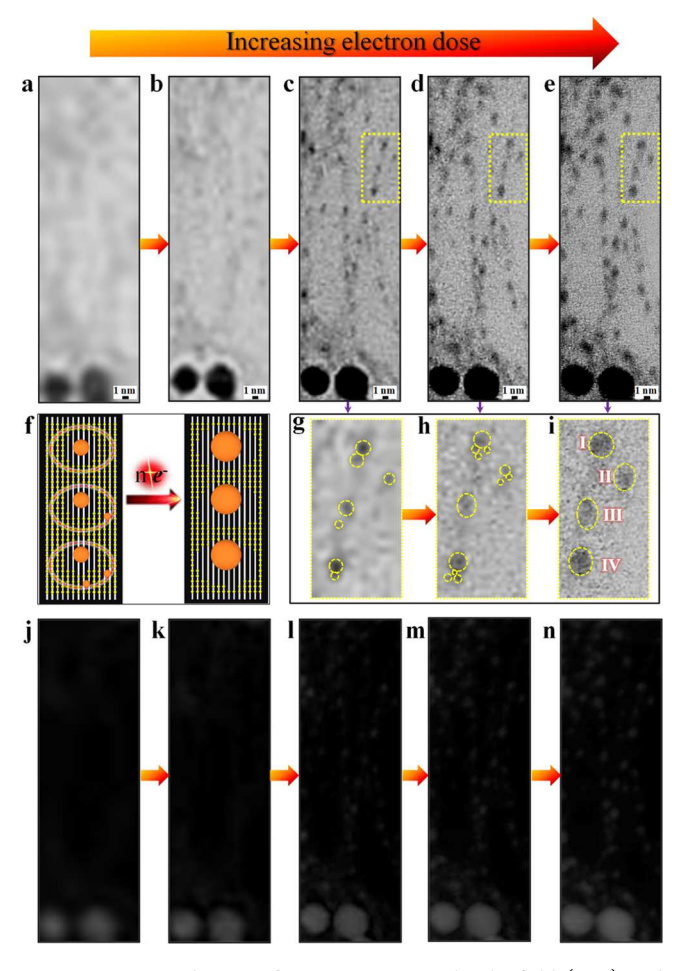


Figure 3. Zoomed areas of STEM images in bright field (a-e) and dark field (j-n) collected by varying the imaging area with fixed current (0.5 nA) and time (8  $\mu$ s/pixel). The experimental imaging areas are  $1.5 \times 10^6$  (a),  $3.8 \times 10^5$  (b),  $9.4 \times 10^4$  (c),  $2.3 \times 10^4$  (d), and  $5.9 \times 10^3$  nm<sup>2</sup> (e), corresponding to electron doses of  $1.1 \times 10^4$ ,  $5.6 \times 10^4$ ,  $2.4 \times 10^5$ ,  $9.6 \times 10^5$ , and  $3.8 \times 10^6$  C/m<sup>2</sup>, respectively. All images share the same scale bar. The bottom two larger-sized particles served as an image contrast reference for the in situ imaging. (f) Illustration of the nucleation and growth under the electron dose. (gi) Magnified images tracking the growth of NPs labeled in regions I, II, III, and IV with electron doses corresponding to those in images (c-e), respectively.

electron doses was also examined. Figure 4a-f,l-q shows a representative set of STEM images (bright and dark field images) to monitor the formation and growth of NCs/NPs which appear in a random distribution area.

The growth profiles for individual NCs/NPs were extracted from the images with different imaging areas where a selected area with a random distribution of NCs/NPs was analyzed using the three larger-sized NPs as an internal reference. The electron dose was controlled by the imaging area, ranging from  $1 \times 10^6$  to  $1 \times 10^3$  nm<sup>2</sup>. Again, no apparent NCs are observed for the imaging area above  $\sim 2 \times 10^6$  nm<sup>2</sup> (Figure 4a,b,l-m). At electron doses larger than that value, NCs/NPs are observed and their sizes show increases with the electron dose (Figure 4c-f,n-q), consistent with those observed for the growth of the NCs/NPs in strings (see Figure 3). Similarly, the NCs/NPs labeled I-V (Figure 4k) show that both aggregative growth and individual growth are operative (Figure 4g-j). The electron dose,  $\sim 1 \times 10^4$  C/m<sup>2</sup> (corresponding to

dose for the imaging area of  $\sim 1 \times 10^6 \text{ nm}^2$ ) could be considered as a threshold for the electron-induced formation of NCs under the experimental conditions.

The structures of the NCs/NPs formed were also examined by HRTEM analysis. As shown in Figure 5, for three indicated areas, highly crystalline structures are evident for the as-formed NCs/NPs (I and III), including the gap between the two larger-sized NPs filled by the grown NCs/NPs (II). The lattice fringes measured in these areas, 0.247-0.253 nm, are characteristic of Au(111) facet, which are essentially the same as those reported for gold NPs prepared by conventional solution synthesis methods.

The growth maps of the NCs/NPs shown in Figures 3 and 4 are further compared to track the overall details in the NC/NP formation, growth, and assembly processes. As illustrated by the schematic evolution in terms of size and distributions (Figure 6a-e), the overall NC/NP size increases with the electron dose, and the particle growth involves individual growth and aggregative growth. The preference assembly in strings is evident.

For the NCs/NPs found in the random distribution area, the schematic evolution shows an increase in size with electron dose in terms of individual and aggregative growth (Figure 6fk), which are qualitatively consistent with those observed for the growth of the NCs/NPs in strings.

The fact that some of the particles appear to grow by its own is suggestive of a pathway involving an initial nucleation of NC followed by deposition of Au atoms on the NC, whereas the growth by aggregation of smaller particles nearby is suggestive of an aggregative growth mechanism.<sup>44</sup> This mechanistic insight is supported by a close examination of NCs/NPs formed in both string and random distribution areas (Figures 3-6).

The size distributions for the NCs/NPs in the strings at different electron doses are shown in Figure 7a. As indicated by the general trend of the size growth as a function of logarithm of electron dose, there is a clear trend for the overall particle size growth. Figure 7b shows the size distributions of the NCs/ NPs in random distributions at different electron doses. There is again a clear indication that the larger-sized particles grow while smaller sized particles disappear.

To further compare the overall growth as a function of electron dose for the formation and growth of NCs/NPs and to compare the growth characteristics between string and random distributions, the growth data from Figure 7a,b are analyzed based on the electron-induced surface reactivity. 45 The intensity (I) of the electron-induced surface reaction, including either direct reduction of Au(I) by electrons or indirect reduction by electron-induced radical species, is expressed by  $I = I_s \times (1 - e^{-\sigma \times D})$ , where  $I_s$  represents the intensity of the reactive electrons at saturation,  $\sigma$  is the cross section for surface reduction of Au(I) by electrons, and D is the surface density of the electron dose. 45 Assuming that the NC/NP growth in terms of particle size (d) is proportional to the particle size growth as a result of the electron-induced surface reduction of Au(I) species, that is,  $d \propto I$ , we have

$$d = C \times (1 - e^{-\sigma \times D}) \tag{3}$$

where C is constant related to the intensity of the reactive electrons. Figure 8 shows a plot of the average size as a function of the total electron dose. As shown by the theoretical fitting of the data, the growth trends for the NCs/NPs in both **ACS Applied Materials & Interfaces** 

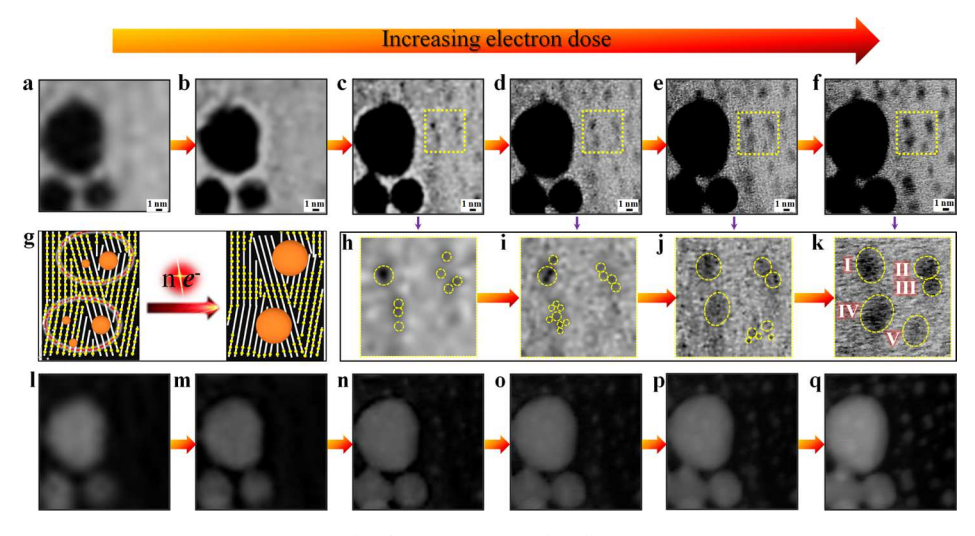


Figure 4. Zoomed areas of STEM images in bright field (a-f) and dark field (l-q) collected by varying the imaging area with fixed current (0.5 nA) and time (8  $\mu$ s/pixel). The experimental imaging areas are 1.5 × 10<sup>6</sup> (a), 3.8 × 10<sup>5</sup> (b), 9.4 × 10<sup>4</sup> (c), 2.3 × 10<sup>4</sup> (d), 5.9 × 10<sup>3</sup> (e), and 1.4 ×  $10^3$  nm<sup>2</sup> (f), corresponding to electron doses of  $1.1 \times 10^4$ ,  $5.6 \times 10^4$ ,  $2.4 \times 10^5$ ,  $9.6 \times 10^5$ ,  $3.8 \times 10^6$ , and  $1.6 \times 10^7$  C/m<sup>2</sup>, respectively. All images share the same scale bar. The lower-left three larger-sized particles served as an image contrast reference for the in situ imaging. (g) Illustration of the nucleation and growth under the electron dose. (h-k) Magnified images tracking the growth of NCs/NPs labeled I-V with electron doses corresponding to those in images (c-f), respectively.

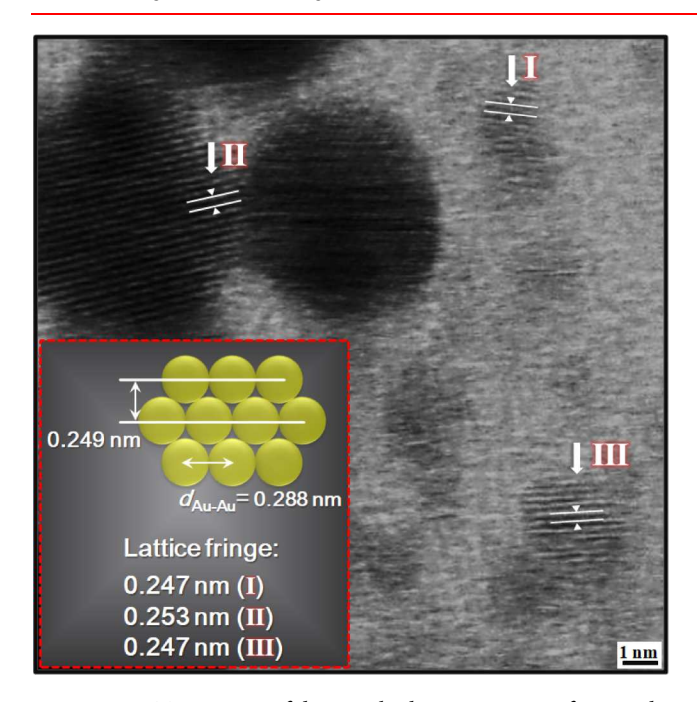


Figure 5. HRTEM image of the sample shown in Figure 4f. Inset: the lattice fringes obtained for the three indicated NC/NP areas.

string and random distributions are quite well described by eq

By comparing the fitting parameters, the results reveal a clear difference in terms of the values of the fitting parameter  $\sigma$ . The apparent cross section for surface reduction of Au(I) by electrons for the growth in the string distribution  $(1.6 \times 10^{-6})$ is greater than that in the random distribution  $(1.1 \times 10^{-6})$ . Clearly, there is a propensity of one-dimensional assembly for the grown NCs/NPs under the electron dose.

Mechanistic Consideration of Growth Mechanism. The propensity of monodispersed NC/NP growth from aurophilic Au(I)-SR motifs under electron dose with welldefined interparticle spacing and one-dimensionality preference is believed to reflect an aggregative growth via a combination of inter- and intra-aurophilic chains of Au-SR motifs, in which the templating force is provided by the electrostatic MPA-/(CTAB)2+2/MPA- (i.e., MPA-···+(CTAB)<sub>2</sub>+···MPA-). This concept is illustrated in Scheme 2.

A key element in the above concept involves two competitive aggregation processes, that is, "interaurophilicchain aggregation" and "intra-aurophilic-chain aggregation". The average interparticle or interstring distance via electrostatic interactions involving MPA<sup>-</sup>/<sup>+</sup>(CTAB)<sub>2</sub><sup>+</sup>/MPA<sup>-</sup> is estimated to be in the range of 3-5 nm, depending on the relative orientation of the molecules (see Scheme S3). There appears to be a close match of this value with the experimental result (3.7 nm) obtained under TEM (see Figure S4a). The measured interparticle spacing along the string (~2 nm, Figure S5) and the fact that the STEM-observed spacing of the highly bundled NC strings ( $\sim$ 1.9 nm, Figure S8) is much smaller than the TEM-observed spacing for the less-bundled NP strings (~3.7 nm) suggest a stronger tendency for the "intraaurophilic aggregation" than that for the "interaurophilic aggregation". In this process, a molecular template is provided by MPA<sup>-</sup>/<sup>+</sup>(CTAB)<sub>2</sub><sup>+</sup>/MPA<sup>-</sup> structure, facilitating the onedimensional assembly of the NCs or NPs. This directional preference is apparently defined by a combination of electrostatic force and aurophilic interaction for the morphological transformation under electron dose. While this mechanism agrees with the formation and growth in a twostage, bottom-up process reported for Au<sub>25</sub> NCs in solutions, <sup>41</sup> which involves a fast reduction and growth followed by a slow conversion between clusters, the electron dose dependence of the NC- and NC-NC aggregative growths demonstrated the viability of both size and assembly control by electron dose to the Au-SR motifs in the molecularly assembled thin film. The latter is supported by a number of theoretical studies, including the study of sequential electron reductions of Au(I)-SR species and the formation of Au<sub>25</sub>(SR)<sub>18</sub>, <sup>41</sup> density functional theory calculation 46 of Au<sub>4</sub> cluster as a basic building unit in the process of growth and size focusing toward the NCs, and a

**ACS Applied Materials & Interfaces** 

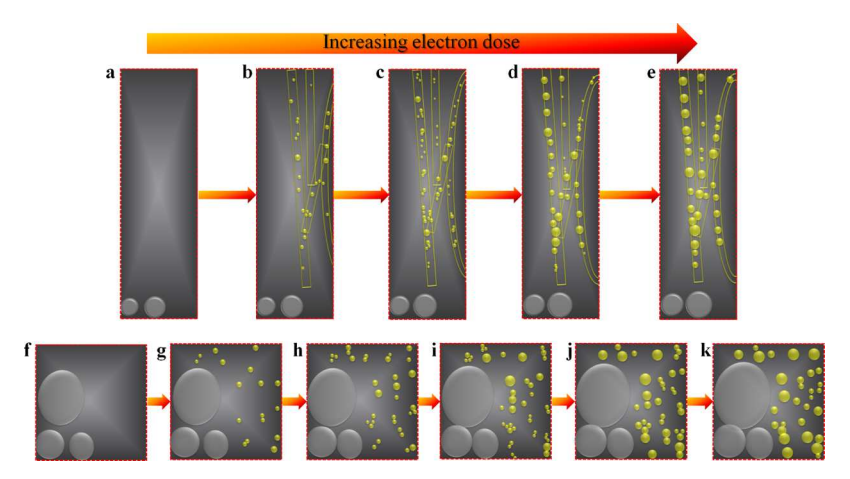


Figure 6. Illustrative mapping of the formation, growth, or assembly of the NCs/NPs under different electron doses. (a–e) Mapping of the data taken from Figure 3 ("string" distribution). (f–k) Mapping of the data taken from Figure 4 ("random" distribution).

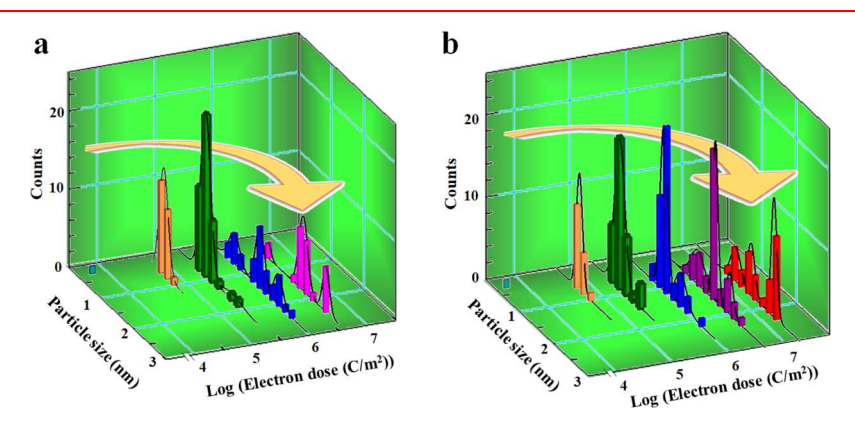
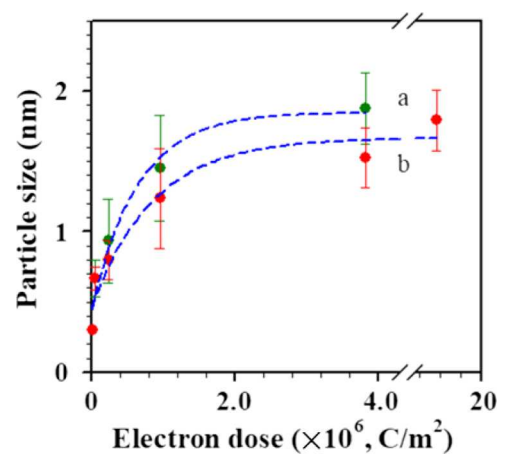


Figure 7. Size distributions of the NCs/NPs [string distribution (a) and random distribution (b)] vs electron dose, for example, taking the data from Figure 3 for (a) (see also Figure S9) and taking the data from Figure 4 for (b) (see also Figure S10).



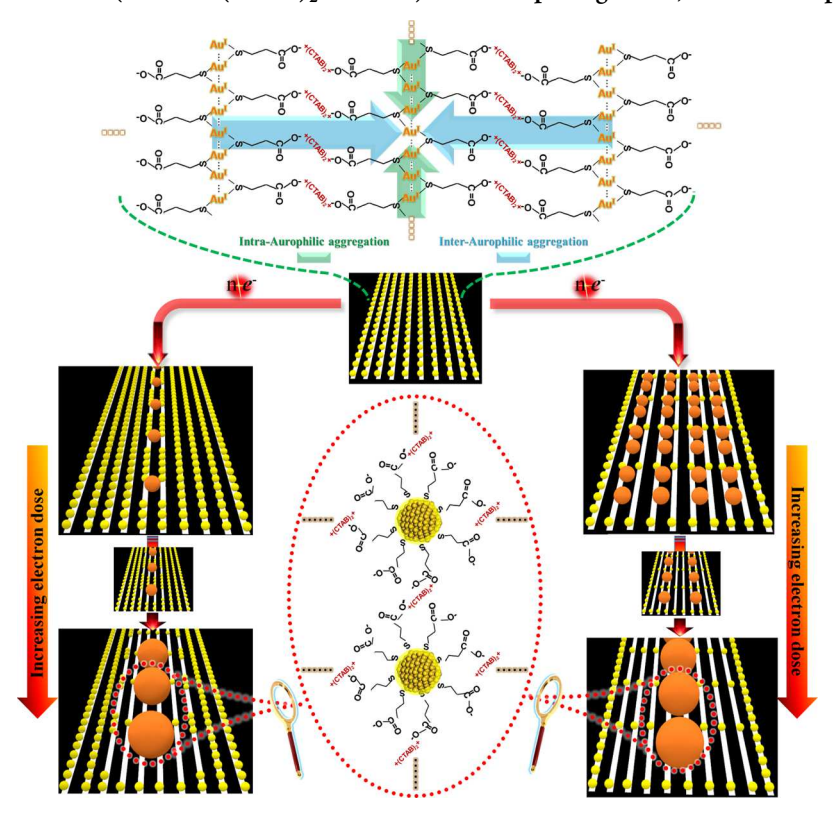
**Figure 8.** Plots of average size distribution of NCs/NPs in STEMstring (a) and random distribution (b) vs the total electron dose in C/m². Dashed lines: the theoretical fit based on the first-order reaction model ( $d = d_{\text{Au}} + C(1 - e^{-\sigma \times D})$ ) yielding  $d_{\text{Au}} = 0.4$ , C = 1.4,  $\sigma = 1.6 \times 10^{-6}$  and R² = 0.9677 (a);  $d_{\text{Au}} = 0.5$ , C = 1.2,  $\sigma = 1.1 \times 10^{-6}$  and  $R^2 = 0.9465$  (b).

sequential two-electron (valence electron) driven LaMer growth (monotonic) and aggregative growth (volcano-shaped) from  $Au_{25}$  NCs to  $Au_{44}$  NPs.<sup>47</sup> Considering that it takes ~30 Au(I), or a small cluster (e.g., ~7  $Au_4$ ), for the formation of a 1 nm NC along and across the aurophilic chains, the aggregative

growth mechanism illustrated in Scheme 2 is not unreasonable. Under electron irradiation, the capping molecules (e.g., MPA-···+(CTAB)2+···MPA-) could form reactive radical intermediates<sup>48</sup> which then reduce Au(I) to Au(0) followed by NC/NP growth. These radicals could undergo carboncarbon bond coupling or oxygenation upon oxidation, but the details are beyond the scope of this report. Nevertheless, the generation of the radical intermediates depends on the electron dose and should display a threshold dose for the resection's occurrence, which is consistent with the observation of a threshold in the electron dose dependences (see Figures 3 and 4). We note that the size distributions in this work are still not very narrow in comparison with those reported in the literature because of limited work on the extensive manipulation of electron dose parameters. The question whether this method can achieve molecular purity in size-focusing synthesis remains to be an interesting topic for future study. In addition, we could only follow the trend of the growth as a function of time in this work. There is a future need to measure the mass quantity of the NCs and NPs in terms of an exactly controlled beam exposure area in STEM experiment to determine the growth efficiency.

#### CONCLUSIONS

Taken together, we have demonstrated a clear electron dose dependence for the electron-driven formation, growth, and one-dimensional assembly of NPs and NCs from aurophilic Scheme 2. Schematic Illustrations of Formation and Assembly of NCs/NPs by Inter-/Intra-Aurophilic Chain Aggregation of Electron-Reduced Au(I)-SR Motifs (See the Top Panel Where the Arrows Illustrate Inter-/Intra-Aurophilic Aggregations with the Electrostatic Interaction (MPA<sup>-...+</sup>(CTAB)<sub>2</sub>+...MPA<sup>-</sup>) as a Templating Force, See Also Top View in Scheme S2)<sup>a</sup>



<sup>a</sup>In the bottom panel, the NC/NP growth is illustrated by either limited nucleation followed by atomic deposition (see left pathway) or by multiple nucleation followed by aggregative growth (see right pathway).

Au(I)—thiolate species in the molecularly assembled thin film. This dependence has been analyzed by in situ monitoring of the nanoscale growth kinetics in terms of the electron dose, which is shown to display a clear preference to a string alignment of the NCs/NPs along the combination of the electrostatic force and the aurophilic interaction, which is shown to reflect a higher cross section of the surface reduction of Au(I) by electrons. The findings have provided new insights into the electron dose-dependent formation, growth, and directional assembly of NCs and NPs on solid surfaces. In addition to 1D assembly, it is possible to use this method to control the structure of NC/NP assembly in different morphologies, for example, 2D or 3D assemblies, by manipulating the ligand chemistry. In view of different possible Au-SR oligomers on Au(111), such as open or cyclic dimers, trimers, and tetramers, <sup>49</sup> the formation of other morphologies of the NC/NP assemblies could also be possible, which should be included in future studies of the electron dose chemistry. In an early density functional theory prediction of a chain structure consisting of Au adatoms and Au-SR complexes on Au(111),50 the complexes were shown to be parallel to each other via linkages formed between Au adatoms and Au atoms in the complexes and via bonding formed between Au adatoms and thiolates. Whether such a structure is operative for the NC/NP assembly in the electron dose chemistry would also be an interesting topic in future studies. The electron dosecontrolled size-focusing and directional assembly of NCs and NPs may be exploited as new strategy for the precise control of NCs or NPs and their assemblies on solid surfaces not only

free from chemical reducing agent but also with the ability of visual monitoring of the morphological evolution during growth, 51 which is important for the design of catalytic sites or sensing interfaces<sup>52</sup> with controlled atomic or nanoscale precision.

# ASSOCIATED CONTENT

# **S** Supporting Information

The Supporting Information is available free of charge on the ACS Publications website at DOI: 10.1021/acsami.8b17941.

Additional results from UV-vis, STEM, EDS, and XPS characterizations, particle size and distribution analysis, and additional schematic illustrations (PDF)

# AUTHOR INFORMATION

#### **Corresponding Authors**

\*E-mail: hwcheng@sit.edu.cn (H.-W.C.).

\*E-mail: cjzhong@binghamton.edu. Phone: 607-777-4605 (C.J.Z.).

# ORCID ®

Chuan-Jian Zhong: 0000-0003-0746-250X

The authors declare no competing financial interest.

# **ACKNOWLEDGMENTS**

The supports by National Science Foundation (IIP 1640669 and CHE 1566283) and in part by DOE-BES grant DE-SC0006877 for this work are acknowledged. The experimental data analyses were in part supported by the NNSFC (grant no. 31800830), Shanghai Sailing Program (16YF1411400), and SIT Program (ZQ2018-26). Part of the work was performed at the Center for Nanoscale Materials, a U.S. DOE Office of Science User Facility and supported by the DOE Office of Science (contract no. DE-AC02-06CH11357).

# **REFERENCES**

- (1) Abedini, A.; Daud, A. R.; Hamid, M. A. A.; Othman, N. K.; Saion, E. A Review on Radiation-induced Nucleation and Growth of Colloidal Metallic Nanoparticles. Nanoscale Res. Lett. 2013, 8, 474.
- (2) Love, J. C.; Estroff, L. A.; Kriebel, J. K.; Nuzzo, R. G.; Whitesides, G. M. Self-Assembled Monolayers of Thiolates on Metals as a Form of Nanotechnology. Chem. Rev. 2005, 105, 1103-1170.
- (3) Pensa, E.; Cortés, E.; Corthey, G.; Carro, P.; Vericat, C.; Fonticelli, M. H.; Benítez, G.; Rubert, A. A.; Salvarezza, R. C. The Chemistry of the Sulfur-Gold Interface: in Search of A Unified Model. Acc. Chem. Res. 2012, 45, 1183-1192.
- (4) Häkkinen, H. The gold-sulfur interface at the nanoscale. Nat. Chem. 2012, 4, 443-455.
- (5) Reimers, J. R.; Ford, M. J.; Marcuccio, S. M.; Ulstrup, J.; Hush, N. S. Competition of van der Waals and chemical forces on goldsulfur surfaces and nanoparticles. Nat. Rev. Chem. 2017, 1, 0017.
- (6) Zhu, M.; Lanni, E.; Garg, N.; Bier, M. E.; Jin, R. Kinetically Controlled, High-yield Synthesis of Au<sub>25</sub> clusters. J. Am. Chem. Soc. 2008, 130, 1138-1139.
- (7) Jin, R.; Zeng, C.; Zhou, M.; Chen, Y. Atomically Precise Colloidal Metal Nanoclusters and Nanoparticles: Fundamentals and Opportunities. Chem. Rev. 2016, 116, 10346-10413.
- (8) Das, A.; Li, T.; Nobusada, K.; Zeng, C.; Rosi, N. L.; Jin, R. Nonsuperatomic [Au<sub>23</sub>(Sc<sub>6</sub>h<sub>11</sub>)<sub>16</sub>] Nanocluster Featuring Bipyramidal Au<sub>15</sub> Kernel and Trimeric Au<sub>3</sub>(Sr)<sub>4</sub> Motif. J. Am. Chem. Soc. 2013,
- (9) Zeng, C.; Li, T.; Das, A.; Rosi, N. L.; Jin, R. Chiral Structure of Thiolate-Protected 28-Gold-Atom Nanocluster Determined by X-Ray Crystallography. J. Am. Chem. Soc. 2013, 135, 10011-10013.
- (10) Zeng, C.; Qian, H.; Li, T.; Li, G.; Rosi, N. L.; Yoon, B.; Barnett, R. N.; Whetten, R. L.; Landman, U.; Jin, R. Total Structure and Electronic Properties of the Gold Nanocrystal Au<sub>36</sub>(SR)<sub>24</sub>. Angew. Chem., Int. Ed. 2012, 51, 13114-13118.
- (11) Antonello, S.; Hesari, M.; Polo, F.; Maran, F. Electron Transfer Catalysis with Monolayer Protected Au<sub>25</sub> Clusters. Nanoscale 2012, 4, 5333-5342.
- (12) Corthey, G.; Giovanetti, L. J.; Ramallo-López, J. M.; Zelaya, E.; Rubert, A. A.; Benitez, G. A.; Requejo, F. G.; Fonticelli, M. H.; Salvarezza, R. C. Synthesis and Characterization of Gold@Gold(I)-Thiomalate Core@Shell Nanoparticles. ACS Nano 2010, 4, 3413-
- (13) Briñas, R. P.; Hu, M.; Qian, L.; Lymar, E. S.; Hainfeld, J. F. Gold Nanoparticle Size Controlled by Polymeric Au(I) Thiolate Precursor Size. J. Am. Chem. Soc. 2008, 130, 975-982.
- (14) Luo, Z.; Yuan, X.; Yu, Y.; Zhang, Q.; Leong, D. T.; Lee, J. Y.; Xie, J. From Aggregation-Induced Emission of Au(I)-Thiolate Complexes to Ultrabright Au(0)@Au(I)-Thiolate Core-Shell Nanoclusters. J. Am. Chem. Soc. 2012, 134, 16662-16670.
- (15) Brown, K.; Parish, R. V.; McAuliffe, C. A. Gold-197 Moessbauer spectroscopic data for antiarthritic drugs and related gold(I) thiol derivatives. J. Am. Chem. Soc. 1981, 103, 4943-4945.
- (16) Bau, R. Crystal Structure of the Antiarthritic Drug Gold Thiomalate (Myochrysine): A Double-Helical Geometry in the Solid State. J. Am. Chem. Soc. 1998, 120, 9380-9381.
- (17) Bachman, R. E.; Bodolosky-Bettis, S. A.; Glennon, S. C.; Sirchio, S. A. Formation of a Novel Luminescent Form of Gold(I) Phenylthiolate via Self-Assembly and Decomposition of Isonitrilegold-(I) Phenylthiolate Complexes. J. Am. Chem. Soc. 2000, 122, 7146-7147.
- (18) Zhou, C.; Sun, C.; Yu, M.; Qin, Y.; Wang, J.; Kim, M.; Zheng, J. Luminescent Gold Nanoparticles with Mixed Valence States

- Generated from Dissociation of Polymeric Au(I) Thiolates. J. Phys. Chem. C 2010, 114, 7727-7732.
- (19) Shaw, C. F. Gold-Based Therapeutic Agents. Chem. Rev. 1999, 99, 2589-2600.
- (20) Wang, P.-p.; Yu, Q.; Long, Y.; Hu, S.; Zhuang, J.; Wang, X. Multivalent Assembly of Ultrasmall Nanoparticles: One-, Two-, and Three-Dimensional Architectures of 2 nm Gold Nanoparticles. Nano Res. 2012, 5, 283-291.
- (21) Lima, J. C.; Rodríguez, L. Supramolecular Gold Metallogelators: The Key Role of Metallophilic Interactions. Inorganics **2015**, 3, 1–18.
- (22) Odriozola, I.; Loinaz, I.; Pomposo, J. A.; Grande, H. J. Gold-Glutathione Supramolecular Hydrogels. J. Mater. Chem. 2007, 17, 4843-4845
- (23) Dreier, T. A.; Ackerson, C. J. Radicals Are Required for Thiol Etching of Gold Particles. Angew. Chem., Int. Ed. 2015, 54, 9249-
- (24) Nimmala, P. R.; Dass, A. Au<sub>99</sub>(SPh)<sub>42</sub> Nanomolecules: Aromatic Thiolate Ligand Induced Conversion of Au<sub>144</sub>(SCH<sub>2</sub>CH<sub>2</sub>Ph)<sub>60</sub>. J. Am. Chem. Soc. **2014**, 136, 17016–17023.
- (25) Brust, M.; Walker, M.; Bethell, D.; Schiffrin, D. J.; Whyman, R. Synthesis of Thiol-Derivatised Gold Nanoparticles in A Two-Phase Liquid-Liquid System. J. Chem. Soc., Chem. Commun. 1994, 801-802.
- (26) Cheng, H.-W.; Wang, J.; Li, Y.-J.; Li, J.; Yan, S.; Shan, S.; Wang, L.; Skeete, Z.; Zhong, C. J. Nanoscale Lacing by Electrons. Small 2018, 14, 1800598.
- (27) Kim, J.-U.; Cha, S.-H.; Shin, K.; Jho, J. Y.; Lee, J.-C. Synthesis of Gold Nanoparticles from Gold(I)-Alkanethiolate Complexes with Supramolecular Structures through Electron Beam Irradiation in TEM. J. Am. Chem. Soc. 2005, 127, 9962-9963.
- (28) Gonzalez-Martinez, I. G.; Bachmatiuk, A.; Bezugly, V.; Kunstmann, J.; Gemming, T.; Liu, Z.; Cuniberti, G.; Rümmeli, M. H. Electron-Beam Induced Synthesis of Nanostructures: A Review. Nanoscale 2016, 8, 11340-11362.
- (29) Wang, B.; Yang, Y. H.; Yang, G. W. Electron-Beam Irradiation Induced Shape Transformation of Sn Sno2 Nanocables. Nanotechnology 2006, 17, 5916-5921.
- (30) Aguiló, E.; Gavara, R.; Lima, J. C.; Llorca, J.; Rodríguez, L. From Au(I) Organometallic Hydrogels to Well-Defined Au(0) Nanoparticles. J. Mater. Chem. C 2013, 1, 5538-5547.
- (31) Dang, Z.; Shamsi, J.; Palazon, F.; Imran, M.; Akkerman, Q. A.; Park, S.; Bertoni, G.; Prato, M.; Brescia, R.; Manna, L. In Situ Transmission Electron Microscopy Study of Electron Beam-Induced Transformations in Colloidal Cesium Lead Halide Perovskite Nanocrystals. ACS Nano 2017, 11, 2124-2132.
- (32) Park, J. H.; Schneider, N. M.; Grogan, J. M.; Reuter, M. C.; Bau, H. H.; Kodambaka, S.; Ross, F. M. Control of Electron Beam-Induced Au Nanocrystal Growth Kinetics through Solution Chemistry. Nano Lett. 2015, 15, 5314-5320.
- (33) Zhang, Y.; Keller, D.; Rossell, M. D.; Erni, R. Formation of Au Nanoparticles in Liquid Cell Transmission Electron Microscopy: From a Systematic Study to Engineered Nanostructures. Chem. Mater. 2017, 29, 10518-10525.
- (34) Spencer, J. A.; Wu, Y.-C.; McElwee-White, L.; Fairbrother, D. H. Electron Induced Surface Reactions of cis-Pt(CO)<sub>2</sub>Cl<sub>2</sub>: A Route to Focused Electron Beam Induced Deposition of Pure Pt Nanostructures. J. Am. Chem. Soc. 2016, 138, 9172-9182.
- (35) Yao, Q.; Chen, T.; Yuan, X.; Xie, J. Toward Total Synthesis of Thiolate-Protected Metal Nanoclusters. Acc. Chem. Res. 2018, 51,
- (36) Chen, T.; Fung, V.; Yao, Q.; Luo, Z.; Jiang, D.-e.; Xie, J. Synthesis of Water-Soluble  $[\mathrm{Au}_{25}(\mathrm{SR})_{18}]^-$  Using a Stoichiometric Amount of NaBH<sub>4</sub>. J. Am. Chem. Soc. 2018, 140, 11370-11377.
- (37) Sau, T. K.; Murphy, C. J. Room Temperature, High-Yield Synthesis of Multiple Shapes of Gold Nanoparticles in Aqueous Solution. J. Am. Chem. Soc. 2004, 126, 8648-8649.
- (38) Nie, H.; Li, M.; Hao, Y.; Wang, X.; Zhang, S. X.-A. Time-Resolved Monitoring of Dynamic Self-Assembly of Au(I)-Thiolate Coordination Polymers. Chem. Sci. 2013, 4, 1852-1857.

- (39) Woehl, T. J.; Evans, J. E.; Arslan, I.; Ristenpart, W. D.; Browning, N. D. Direct In Situ Determination of the Mechanisms Controlling Nanoparticle Nucleation and Growth. *ACS Nano* **2012**, *6*, 8599–8610.
- (40) Puster, M.; Rodríguez-Manzo, J. A.; Balan, A.; Drndić, M. Toward Sensitive Graphene Nanoribbon–Nanopore Devices by Preventing Electron Beam-Induced Damage. *ACS Nano* **2013**, *7*, 11283–11289.
- (41) Luo, Z.; Nachammai, V.; Zhang, B.; Yan, N.; Leong, D. T.; Jiang, D.-e.; Xie, J. Toward Understanding the Growth Mechanism: Tracing All Stable Intermediate Species from Reduction of Au(I)-thiolate Complexes to Evolution of Au<sub>25</sub> Nanoclusters. *J. Am. Chem. Soc.* 2014, 136, 10577–10580.
- (42) Gonzalez-Martinez, I. G.; Bachmatiuk, A.; Bezugly, V.; Kunstmann, J.; Gemming, T.; Liu, Z.; Cuniberti, G.; Rümmeli, M. H. Electron-beam induced synthesis of nanostructures: a review. *Nanoscale* **2016**, *8*, 11340–11362.
- (43) Cazaux, J. Correlations between ionization radiation damage and charging effects in transmission electron microscopy. *Ultramicroscopy* 1995, 60, 411–425.
- (44) Wang, F.; Richards, V. N.; Shields, S. P.; Buhro, W. E. Kinetics and Mechanisms of Aggregative Nanocrystal Growth. *Chem. Mater.* **2014**, *26*, 5–21.
- (45) Klyachko, D. V.; Rowntree, P.; Sanche, L. Dynamics of Surface Reactions Induced by Low-energy Electrons Oxidation of Hydrogen-passivated Si by H<sub>2</sub>O. *Surf. Sci.* **1997**, *389*, 29–47.
- (46) Liu, C.; Pei, Y.; Sun, H.; Ma, J. The Nucleation and Growth Mechanism of Thiolate-Protected Au Nanoclusters. *J. Am. Chem. Soc.* **2015**, *137*, 15809–15816.
- (47) Yao, Q.; Yuan, X.; Fung, V.; Yu, Y.; Leong, D. T.; Jiang, D. E.; Xie, J. Understanding Seed-Mediated Growth of Gold Nanoclusters at Molecular Level. *Nat. Commun.* **2017**, *8*, 927.
- (48) Marqués-Hueso, J.; Abargues, R.; Canet-Ferrer, J.; Agouram, S.; Valdés, J. L.; Martínez-Pastor, J. P. Au-PVA Nanocomposite Negative Resist for One-Step Three-Dimensional e-Beam Lithography. *Langmuir* **2010**, *26*, 2825–2830.
- (49) Jiang, D.-e.; Dai, S. Constructing Gold—Thiolate Oligomers and Polymers on Au(111) Based on the Linear S—Au—S Geometry. *J. Phys. Chem. C* **2009**, *113*, 7838—7842.
- (50) Jiang, D.-e. Au adatom-linked CH<sub>3</sub>S-Au-SCH<sub>3</sub> complexes on Au(111). Chem. Phys. Lett. **2009**, 477, 90-94.
- (51) Lu, A.; Peng, D. L.; Chang, F.; Skeete, Z.; Shan, S.; Sharma, A.; Luo, J.; Zhong, C. J. Composition- and Structure-Tunable Gold—Cobalt Nanoparticles and Electrocatalytic Synergy for Oxygen Evolution Reaction. ACS Appl. Mater. Interfaces 2016, 8, 20082—20091.
- (52) Cheng, H. W.; Yan, S.; Han, L.; Chen, Y.; Kang, N.; Skeete, Z.; Luo, J.; Zhong, C. J. Chemiresistive Properties Regulated by Nanoscale Curvature in Molecularly-linked Nanoparticle Composite Assembly. *Nanoscale* **2017**, *9*, 4013–4023.
- (53) Antonello, S.; Arrigoni, G.; Dainese, T.; De Nardi, M.; Parisio, G.; Perotti, L.; René, A.; Venzo, A.; Maran, F. Electron Transfer through 3D Monolayers on Au25 Clusters. ACS Nano 2014, 8, 2788–2795.